1-1-2020

Supercritical CO2-constructed intralayer $[Bi2O2]^{2+}$structural distortion for enhanced CO2 electroreduction

Yannan Zhou

Pengfei Yan

Jun Jia

Suoying Zhang

Xiaoli Zheng

See next page for additional authors

Supercritical CO2-constructed intralayer $[Bi2O2]^{2+}$structural distortion for enhanced CO2 electroreduction

Abstract

© 2020 The Royal Society of Chemistry. Inducing crystal distortion in two-dimensional (2D) materials to increase the number of active sites is of great significance in improving the intrinsic activity of electrocatalysts for the CO2 reduction reaction (CO2RR). Developing 2D materials as thin as possible is required for this goal. Herein, taking layered BiOCl as a prototype model, we achieved the intralayer [Bi2O2]2+ structural distortion by using supercritical CO2 as a solvent to reduce the number of interlayer chlorine atoms involved in the reaction. Contrary to expectations, further CO2RR experiments indicate that thick nanoplates exhibit a high faradaic efficiency of ~92% for conversion of CO2 to formate in a wide potential window, whereas ultrathin nanosheets mainly produce H2. Density functional theory calculation shows that increased [Bi2O2]2+ structural distortion in thick nanoplate layers is responsible for the finding. This strategy provides a new route to promoting the intrinsic activity of electrocatalysts, and provides us with a new insight into understanding thickness-dependent activity.

Keywords

intralayer, co2-constructed, electroreduction, supercritical, co2, enhanced, distortion, [bi2o2]2+structural

Disciplines

Engineering | Physical Sciences and Mathematics

Publication Details

Zhou, Y., Yan, P., Jia, J., Zhang, S., Zheng, X., Zhang, L., Zhang, B., Chen, J., Hao, W., Chen, G., Xu, Q. & Han, B. (2020). Supercritical CO2-constructed intralayer $[Bi2O2]^{2+}$structural distortion for enhanced CO2 electroreduction. Journal of Materials Chemistry A, 8 (26), 13320-13327.

Authors

Yannan Zhou, Pengfei Yan, Jun Jia, Suoying Zhang, Xiaoli Zheng, Li Zhang, Bin Zhang, Jun Chen, Weichang Hao, Gongji Chen, Qun Xu, and Buxing Han

Supercritical CO_2-constructed intralayer $[Bi_2O_2]^{2+}$ structural distortion for enhanced CO_2 electroreduction†

Yannan Zhou,‡[a] Pengfei Yan,‡[a] Jun Jia,[a] Suoying Zhang,[c] Xiaoli Zheng,[a] Li Zhang,[a] Bin Zhang,[a] Jun Chen,[d] Weichang Hao,[e] Gongji Chen,[f] Qun Xu*[ab] and Buxing Han*[g]

Inducing crystal distortion in two-dimensional (2D) materials to increase the number of active sites is of great significance in improving the intrinsic activity of electrocatalysts for the CO_2 reduction reaction (CO_2RR). Developing 2D materials as thin as possible is required for this goal. Herein, taking layered BiOCl as a prototype model, we achieved the intralayer $[Bi_2O_2]^{2+}$ structural distortion by using supercritical CO_2 as a solvent to reduce the number of interlayer chlorine atoms involved in the reaction. Contrary to expectations, further CO_2RR experiments indicate that thick nanoplates exhibit a high faradaic efficiency of ~92% for conversion of CO_2 to formate in a wide potential window, whereas ultrathin nanosheets mainly produce H_2. Density functional theory calculation shows that increased $[Bi_2O_2]^{2+}$ structural distortion in thick nanoplate layers is responsible for the finding. This strategy provides a new route to promoting the intrinsic activity of electrocatalysts, and provides us with a new insight into understanding thickness-dependent activity.

Introduction

The electrocatalytic CO_2 reduction reaction (CO_2RR) powered by renewable electricity represents a promising and viable strategy to transform CO_2 into valuable carbon-based chemicals such as formate.[1–5] For the formation of formate, the initial activation of stable CO_2 molecules and the binding strength of reaction intermediates on the catalyst surface determine the activity and selectivity of the CO_2RR.[6–10] A series of studies on the surface atomic and electronic structure of electrocatalysts have clearly shown that the binding energy for reaction intermediates is closely affiliated with defect engineering such as crystal distortion.[11–13] To date, numerous approaches have been explored to construct crystal distortion in two-dimensional (2D) catalysts. Examples include introducing active heteroatomic dopants, stretching support substrates, reducing thickness to the sub-nanometer scale, and ion intercalation.[14,15] Among them, developing 2D catalysts as thin as possible can create various degrees of crystal distortion, and it is recognized that ideal 2D catalysts with a single atomic layer thickness exhibit optimal intrinsic activity.[16,17] However, the thickness-dependent-structural distortion in layered 2D catalysts and the correlated intrinsic activity have rarely been investigated experimentally or theoretically.

Here, a novel method utilizing supercritical carbon dioxide (SC CO_2) and water as a solvent mixture to construct intralayer structural distortion in layered 2D catalysts with various thicknesses has been explored. Typical layered bismuth oxychloride (BiOCl) in which each [BiOCl] monolayer consisting of $[Bi_2O_2]^{2+}$ slabs being sandwiched between chlorine ion layers,[18] as the model material, was chosen for the study. The introduced SC CO_2 molecules can penetrate the framework of layered BiOCl with decreased surface tension and capillary forces, and further reduce the number of Cl atoms involved in the reaction by phase transition from SC CO_2 to gaseous CO_2. Density functional theory (DFT) calculation shows that the decreased number of interlayer Cl atoms can help achieve the intralayer

[a]College of Materials Science and Engineering, Zhengzhou University, Zhengzhou 450052, P. R. China. E-mail: qunxu@zzu.edu.cn

[b]Henan Institute of Advanced Technology, Zhengzhou University, Zhengzhou 450052, P. R. China

[c]Key Laboratory of Flexible Electronics (KLOFE), Institute of Advanced Materials (IAM), Nanjing Tech University (Nanjing Tech), 30 South Puzhu Road, Nanjing 211816, P. R. China

[d]Intelligent Polymer Research Institute (IPRI), ARC Centre of Excellence for Electromaterials Science (ACES), Australian Institute for Innovative Materials (AIIM), Innovation Campus, University of Wollongong, Squires Way, North Wollongong, NSW 2519, Australia

[e]Center of Materials Physics and Chemistry, Department of Physics, Beihang University, Beijing 100191, P. R. China

[f]Supercomputing Center, Zhengzhou University, Zhengzhou 450052, P. R. China

[g]Beijing National Laboratory for Molecular Sciences, Key Laboratory of Colloid and Interface and Thermodynamics, Institute of Chemistry, Chinese Academy of Sciences, Beijing 100190, P. R. China. E-mail: hanbx@iccas.ac.cn

$[Bi_2O_2]^{2+}$ structural distortion, which can act as active sites for the adsorption and activation of CO_2 molecules. Further Gibbs free energy calculations on different reaction pathways of the CO_2RR show that thick nanoplates exhibit a higher activity and selectivity for formate formation than ultrathin nanosheets under identical degree of Cl atom deficiency due to the increased intralayer structural distortion.

Consistent with theoretical analysis, the designed BiOCl nanoplates (~17 layers) with intralayer $[Bi_2O_2]^{2+}$ structural distortion can boost the conversion of CO_2 molecules to formate in a low and broad potential window (−0.6 to −0.9 V *vs.* RHE) with high selectivity (92%) and a formate partial current density of 28.63 mA cm^{-2} mg^{-1} at −0.9 V *vs.* RHE. In contrast, distorted ultrathin BiOCl nanosheets (~5 layers) mainly produced H_2 at these potentials, and standard BiOCl nanoplates (~15 layers) without intralayer $[Bi_2O_2]^{2+}$ structural distortion showed lower activity and selectivity for formate formation. Here it is noteworthy that this strategy can help us accomplish closed recycling between catalyst preparation and selective CO_2 reduction to valuable chemical products.

Experimental section

Chemicals and materials

All the chemicals were purchased from Shanghai Macklin Biochemical Co., Ltd and used without any further purification, including $Bi(NO_3)_3$\$$5H_2O$ (99%), NaCl (99.5%), mannitol (99%), and $KHCO_3$ (99.97%). CO_2 and Ar with a purity of 99.99% were purchased from Zhengzhou Shuangyang Gas Co., Ltd.

Preparation of distorted BiOCl nanoplates

In a typical synthesis of distorted BiOCl nanoplates, 0.5 mmol of $Bi(NO_3)_3$\$$5H_2O$ (0.243 g) was dissolved in 10 mL of 0.1 M mannitol solution under vigorous stirring for 30 min to obtain a transparent solution. Then, 0.5 mmol NaCl was slowly added into the above solution, and a uniform milky suspension was quickly produced. After a 30 min agitation, the formed suspension was transferred into a supercritical CO_2 apparatus composed mainly of a stainless-steel autoclave with a heating jacket and a temperature controller. The autoclave was heated to 160 °C, and then CO_2 was charged into the reactor to 20 MPa for 3 h under continuous stirring. After the CO_2 was slowly released, the product was collected by centrifugation at 8000 rpm. for 10 min, washed with deionized water three times, and then dried at 60 °C under vacuum. The final sample was denoted as distorted BiOCl.

Preparation of standard BiOCl nanoplates

Standard BiOCl without intrinsic defects was prepared as a reference catalyst, following the above method of distorted BiOCl but without SC CO_2 treatment.

Preparation of ultrathin BiOCl nanosheets

0.5 mmol of $Bi(NO_3)_3$\$$5H_2O$ (0.243 g) and 0.2 g of polyvinylpyrrolidone were dissolved in 10 mL of 0.1 M mannitol solution and stirred for 30 min. Then, 0.5 mmol of NaCl was slowly added and stirred for another 30 min. Subsequently, the resultant suspension was subjected to the same SC CO_2 treatment as distorted BiOCl nanoflakes. After centrifugation and drying, the obtained product was denoted as another reference catalyst (ultrathin BiOCl nanosheets).

Electrochemical CO_2 reduction reaction (CO_2RR)

The CO_2RR activities of the target samples were evaluated using a standard three-electrode system connected to an electrochemical workstation (CHI660E). Pt foil and a Ag/AgCl electrode (saturated KCl) were respectively used as counter and reference electrodes and separated by a Nafion 211 membrane to avoid the re-oxidation of the products on the counter electrode. The applied electrode potentials were converted to the RHE scale based on the following equation: $E_{RHE} = E_{Ag/AgCl} + 0.197\ V + 0.059 \times pH$. To prepare the working electrodes, a suspension containing 3 mg of the target catalyst and 1 mg carbon powder, 10 mL of 5 wt% Nafion solution, 440 mL of alcohol and 450 mL (18.2 MU cm^{-1}) of deionized water (MQ-grade, Millipore) was used. After sonication for 2 h, 300 mL of coating ink was dispersed on one side of carbon paper (1 cm × 1 cm) and dried at 60 °C. And the actual mass loading for the electrochemical test was 1 mg cm^{-2}; the current density reported in this work was normalized to the geometric area and unit mass.

In a typical CO_2RR process, 30 mL of 0.5 M $KHCO_3$ electrolyte was allowed to flow in the cathode and anode chambers, and a headspace of about 20 mL was left. Before electrolysis, CO_2 gas was bubbled for 30 minutes at a rate of 20 mL min^{-1} *via* a mass flow controller (GFC17, Aalborg) and continuously fed in the whole process of electrolysis. After 30 min of CO_2 electrolysis at constant working potential, the gaseous products were analyzed and quantified by an external standard method through gas chromatograph with a thermal conductivity detector (for H_2) and a flame ionization detector (for CO, CH_4, C_2H_4 *etc.*). In addition, the electrolyte after the reaction was analysed using HNMR spectra; 0.49 mL of the electrolyte mixed with 0.1 mL of D_2O and 0.01 mL of dimethyl sulfoxide (DMSO) was added as an internal standard (600 MHz NMR spectrometer, Bruker). The concentration of formate was quantitatively determined from its NMR peak area relative to that of the internal standard using the calibration curve from a series of standard HCOONa solutions.

$$FE = 2F \times \frac{n_{formate}}{Q} = 2F \times \frac{n_{formate}}{I \times t}$$

where F is the Faraday constant, I is the current density, t is the electrolysis time, and $n_{formate}$ is the total amount of formate (in moles). All the electrolysis experiments were conducted at room temperature without iR correction.

ECSA measurements

The electrochemical double-layer capacitance of the catalyst surface was measured using non-faradaic capacitive current associated with double-layer charging from the scan-rate dependence of cyclic voltammograms. The electrochemically active surface area (ECSA) was further calculated from the

electrochemical capacitance to evaluate the intrinsic activity of standard BiOCl and distorted BiOCl nanoplates.

Geometric phase analysis of strain fields

Geometric phase analysis was performed with DigitalMicrograph using Koch's FRWR tools plugin, which is based on the methods of Hÿtch *et al.*[19,20] GPA phase maps and strain fields ε_{xx}, ε_{yy}, ε_{xy}, and the rotation ω (radians) are obtained from Bragg spots in the corresponding FFT. The color scale of the phase maps is from black (−p) to white (−p). The strain colour scale corresponds to a range from −50% (black) to 50% (white).

Results and discussion

Theoretical prediction of intralayer $[Bi_2O_2]^{2+}$ structural distortion formation and activation

Different from common transition-metal dichalcogenides, the supercell model of the BiOCl (200) surface is shown in Fig. S1†. Once the van der Waals interaction between $[Bi_2O_2]^{2+}$ and $[Cl]^-$ layers is broken, Bi and O atoms in the layers will be directly exposed and might act as active sites for conversion of CO_2 to formate. Herein, the interlayer interaction is affected by removal of Cl atoms and the resulting structures are relaxed and fully optimized using DFT. It is found out that with the increase of Cl atom removal, progressively distorted intralayer $[Bi_2O_2]^{2+}$ structures can be formed, therefore promoting CO_2 molecule adsorption and activation (Fig. 1 and S2†). In fact, CO_2 molecules cannot adsorb on the surface of perfect BiOCl. A large amount of atomic charge analysis and orbital population analysis reveal that Bi atoms on a distorted surface will gain more electrons when they are localized to the p orbital (Fig. S3 and Table S1†). Furthermore, as the number of removed Cl atoms increases, Bi atoms on the distorted structure can provide more electrons for activating CO_2 molecules, which can be indicated by the reduced bond angle from an initial value of 180° to ~125.6° (Fig. S4a†). Importantly, different from that of traditional single-metal active sites, the varying charge density on multiple configurations demonstrates that Bi and O atoms on the distorted surface have a synergistic effect on the adsorption and activation of CO_2 molecules (Fig. S4b†). In particular, the intralayer $[Bi_2O_2]^{2+}$ distorted structure can anchor and adsorb CO_2 molecules through bonding between O atoms and C atoms, and then Bi atom supplies sufficient electrons to activate CO_2 (Fig. S4c†). Once enough Cl atoms are removed, stable intralayer adsorption configurations of CO_2 molecules can be formed (configuration 3 and 4). And it is reasonably speculated that thicker catalysts should exhibit higher activity than the thinner ones because more intralayer $[Bi_2O_2]^{2+}$ can be distorted and activated.

Structural characterization of structural distortion

According to the theoretical prediction above, supercritical CO_2 (SC CO_2) was used to help synthesize distorted thick BiOCl nanoplates and ultrathin BiOCl nanosheets for the purpose of constructing and comparing thickness-dependent activity. And at the same time, the standard BiOCl nanoplates without intralayer distortion were also prepared for the control experiment. The XPS spectra of standard BiOCl and distorted BiOCl nanoplates validate the existence of bismuth, oxygen, chlorine and carbon (Fig. S5†). Compared to the single oxidation state of

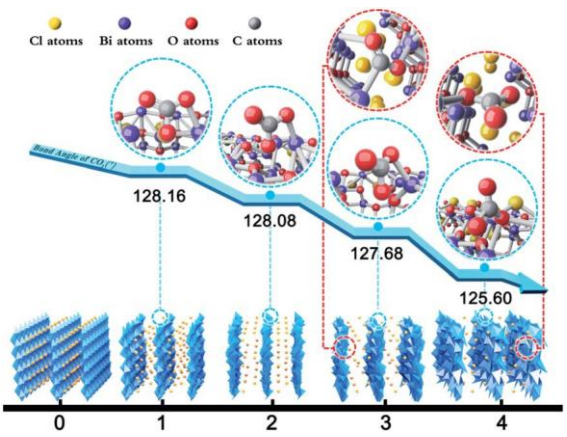

Fig. 1 Theoretical calculation. Structural configurations of BiOCl with different Cl atom removed layers (1–4) and the corresponding CO_2 adsorption configurations and adsorption parameters; blue tetrahedron: $[Bi_2O_2]^{2+}$, blue circle: surface adsorption, and red circle: intralayer adsorption.

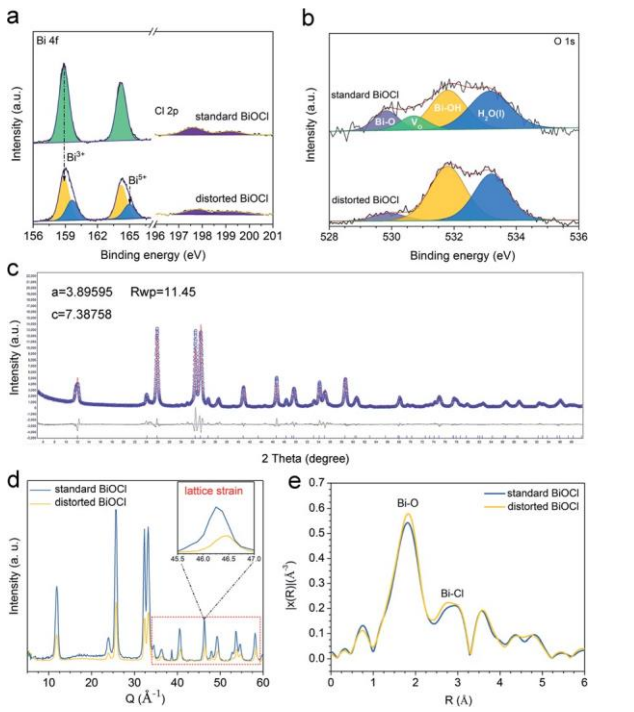

Fig. 2 Structural characterization of standard BiOCl and distorted BiOCl nanoplates. (a) High-resolution XPS spectra of Bi 4f and Cl 2p. (b) O 1s high-resolution XPS spectra. (c) Rietveld refinement plots of the powder X-ray diffraction data of distorted BiOCl nanoplates in the tetragonal space group *P*4/*nmm*. Observed data: blue circle; calculated intensities: red line; difference: gray lines and allowed Bragg reflections: bottom ticks. (d) WAXS patterns plotted as a function of the momentum transfer *Q*, inset: partially enlarged detail. (e) Raw results of the EXAFS spectra in *R* space.

Bi^{3+} in standard BiOCl nanoplates, the two new emerging signals at 159.65 and 165.00 eV of distorted BiOCl nanoplates indicate the existence of Bi^{5+} (Fig. 2a).[21] The high-resolution O 1s spectra (Fig. 2b) further shed light on the peculiarity of the SC CO_2-treated samples. The binding energies of 529.85, 531.75 and 533.15 eV can be assigned to lattice oxygen (Bi–O), Bi–OH and chemisorbed water, respectively.[22] For the standard BiOCl nanoplates, the characteristic peak at 530.70 eV indicates that surface oxygen vacancies exist, while it is absent for the distorted BiOCl nanoplates.[18] And the disappearance of surface oxygen vacancies is due to the adsorption of CO_2 solvent molecules, which not only insert one of their O atoms into the oxygen vacancy site, but also accept electrons from Bi^{3+} to form a bent CO^{2-} species.[23] Further the atomic ratio of Cl atoms in distorted BiOCl nanoplates decreases by 20 percent compared to that of standard BiOCl nanoplates, indicating the occurrence of interlayer Cl atom deficiency (Fig. 2a). So it can be concluded that distorted BiOCl nanoplates fabricated using SC CO_2 only present interlayer Cl defects, and the resultant structural distortion is the principal factor that influences the following performance of the CO_2RR.

As shown in Fig. S6†, both the as-prepared nanoplates possess a square-like morphology with a uniform particle size and thickness. Compared with standard BiOCl nanoplates, a noticeable color transformation from white to yellow for distorted BiOCl nanoplates can be observed, and the decreased diffraction peak intensity of distorted BiOCl nanoplates is shown in Fig. S6c†. So an intrinsic defect structure might be existing.[24,25] Detailed structural analyses based on the powder XRD patterns of the distorted BiOCl nanoplates are performed as shown in Fig. 2c. The Rietveld refinement plots showing tetragonal symmetry with the $P4/nmm$ space group are displayed, and the lattice parameters are $a = b = 3.8959(5)$ Å, $c = 7.3875(8)$ Å, and $v = 112.26$ Å^3. Further, the wide-angle X-ray scattering (WAXS) patterns are obtained to reveal the local crystal distortion induced by interlayer Cl deficiency coming from SC CO_2 (Fig. 2d). And the shift of X-ray reflection peaks toward a higher Q value is attributed to the macrostrain caused by the change of the whole Bi : O : Cl atomic ratio.[12,26] Moreover the apparently broadened peaks at high Q values indicate the existence of structural defects in distorted BiOCl nanoplates again.[12] The XRD pattern of ultrathin BiOCl nanosheets could also be well indexed to the tetragonal phase of BiOCl (Fig. S6d†).

In order to probe the local electronic structure of distorted BiOCl nanoplates, X-ray absorption near edge structure (XANES) and extended X-ray absorption fine structure (EXAFS) are operated and their results are shown in Fig. S7† and 2e. The Bi L-edge of the XANES spectrum of distorted BiOCl shows no obvious shift toward higher energy compared with that of standard BiOCl nanoplates, demonstrating that Bi^{5+} only exists on the surface. The Fourier transformed $|c(R)|$ spectrum is obtained to evaluate the density of neighboring Cl atoms as a function of radial distance. The fitted spectra and parameters are displayed in Fig. S7b and Table S2.† Apparently, the distorted BiOCl nanoplates show a higher density of Bi–O bonds and a reduced Bi–Cl coordination number (CN: 3.6) compared to standard BiOCl (CN: 4), and this is in accordance with the theoretical prediction. Notably, an enhanced bismuth–oxygen structure in the Bi composites can help to promote the selective CO_2 reduction towards formate production.[27]

Microscopic characterization of structural distortion

The morphology of standard BiOCl, distorted BiOCl nanoplates and ultrathin BiOCl nanosheets is shown in Fig. S8–S11†, respectively. Distorted BiOCl nanoplates synthesized using SC CO_2 maintain the intact layered structures. The square-like morphology of distorted BiOCl with average lateral diameters of ~50 nm and thicknesses of 13 nm (~17 layers) are presented in Fig. S9†. Compared with those of the standard BiOCl nanoplates in Fig. S8† (~15 layers), the visible roughness and pores on the surface of distorted BiOCl could be one positive factor in CO_2 adsorption. The discrete elemental mapping images of Bi, O and Cl atoms of a single nanoplate in Fig. S9d† further demonstrate the rough surface of distorted BiOCl nanoplates. The AFM image and the corresponding height profile of ultrathin BiOCl nanosheets in Fig. S10† confirm that the thickness of the nanosheets is ~3.80 nm (~5 layers). Further high-angle annular dark-field scanning transmission electron microscopy (HAADF-STEM) images (Fig. 3a, d and g) are employed to display the detailed local structural distortion in distorted BiOCl nanoplates. The Bragg filtered images of the lattice fringe reflection enclosed by a blue square clearly display the structural distortion. Fig. 3b expresses a cross-sectional lattice expansion in the strained layer and Fig. 3e presents the discontinuities of (101) crystal planes. Further, the notably distorted $[Bi_2O_2]^{2+}$ structure in the [002] projection is depicted in Fig. 3h.

Usually, the dislocation field can introduce considerable levels of strain that can significantly influence the CO_2RR

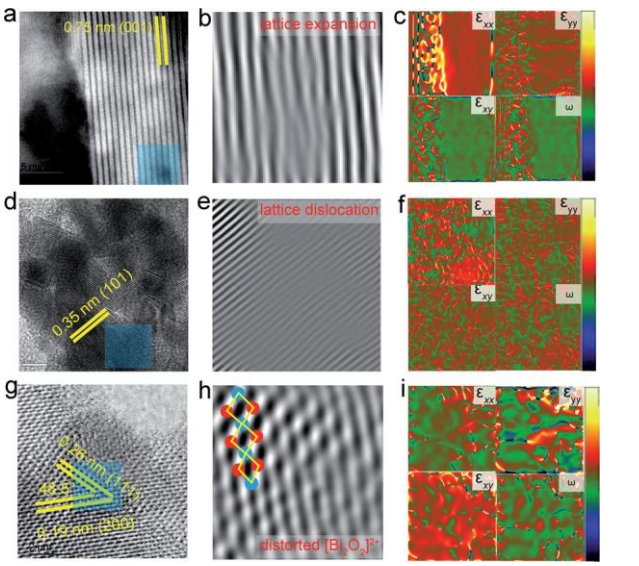

Fig. 3 Microscopic characterization of distorted BiOCl nanoplates. (a, d and g) High-magnification STEM images, and (b, e and h) Bragg filtered images of the lattice fringe reflection enclosed by blue square highlighting the structural distortion. (c, f and i) Strain maps of 3_{xx}, 3_{yy}, and 3_{xy} and the rotation u on different Bragg spots, and the strain color scales with a range from −50% (black) to 50% (white).

activity.[24] Geometric phase analysis (GPA) was used to map the spatially distributed strain fields around dislocations.[20,28] The strain maps of ε_{xx} (in-plane), ε_{yy} (out-of-plane), and ε_{xy} (shear strain), and the rotation ω generated from respective Bragg spots in FFT images (Fig. S12†) are shown in Fig. 3c, f and i. The in-plane ε_{xx} map of the (001) phase suggests an average tensile lattice strain around 5% due to a relatively large lattice expansion. Furthermore, as expected in DFT analysis, the intralayer $[Bi_2O_2]^{2+}$ structural distortion can be further evidenced using the fluctuant out-of-plane ε_{yy} maps (parallel to the 001 direction). Furthermore, compared to the (001) lattice plane, high-index facets such as (101) and (200) show enhanced compressive and tensile strains ranging from −10% to 20% and they coexist in ε_{xx}, ε_{yy}, and ε_{xy} maps. The quantitative strain fluctuation of GPA analysis agrees well with the foregoing WAXS results, indicating that the larger lattice strain comes from the high-angle lattice distortion. And this peculiar phenomenon can be attributed to the SC CO_2-simulated activation of high-index facets. Obviously, the complex strain effect induced by SC CO_2 differs from conventional strain introduction approaches such as using high-pressure. In contrast, a similar structural distortion exists in BiOCl ultrathin nanosheets (Fig. S11†) while it disappears in standard BiOCl nanoplates (Fig. S8†), and this can further indicate the crucial role of SC CO_2 in developing intralayer structural distortion.

Comparison of the activity and selectivity of standard BiOCl, distorted BiOCl nanoplates and ultrathin BiOCl nanosheets

Positively charged Bi^{n+} on distorted BiOCl nanoplates. The CO_2 electroreduction activities and product selectivity are tested for the three prototype model catalysts, and they are evaluated in CO_2-saturated 0.5 M $KHCO_3$ (pH ¼ 7.52) electrolyte. Different from previous reports,[29,30] the theoretical cathodic peak of distorted BiOCl nanoplates triggered by electrochemical reduction of Bi^{3+} to Bi^0 cannot be detected during negative sweep between −1.2 and 0 V (*vs.* RHE) (Fig. S13a†). Instead, a pronounced cathodic peak at −0.55 V appears in the long-term cyclic voltammetry (CV) curve between −1.2 and 1.2 V, and the peak gradually shifts toward a more positive potential during negative sweep (Fig. S13b†). According to the Pourbaix diagram of Bi in H_2O,[31] the first pair of symmetric redox waves may be contributed by the interconversion of Bi^{5+} to Bi^0. After reaction for 11 h, the final cathodic peak appears at −0.26 V which is still more negative than the reduction potential of Bi^{3+} to Bi^0 (−0.14 V),[30,32] indicating that positively charged Bi^{n+} ($3 < n < 5$) active species still exist in the catalyst. This phenomenon could be caused by the continuous electron transfer from Bi atoms to CO_2 molecules. On this basis, zeta potential (Fig. S14†) is recorded to evaluate the surface charge. The zeta potential values of standard BiOCl and distorted BiOCl nanoplates are −17.90 and −24.90 mV in 0.5 M $KHCO_3$ aqueous solution, respectively, and the negative charge could be due to the adsorption of dominant bicarbonate ions on the sliding layer of the particle double electric layer. And the more negative zeta potential value of distorted BiOCl indicates the more positive charge on its particle surface. Apparently the positively charged active sites on distorted BiOCl nanoplates can facilitate the activation and protonation of CO_2 through stabilizing CO_2c^- and $HCOO^-$.[6,9,33]

The key role of structural distortion in thick nanoplates. The recorded polarization curves of standard BiOCl and distorted BiOCl nanoplates in Ar- (to avoid the effect of N_2 reduction during electrocatalysis) and CO_2-saturated electrolytes at a scan rate of 20 mV s^{-1} indicate that they both are active for the CO_2RR. The cathodic current disruption of distorted BiOCl occurs at −0.51 V, which is more positive than that of the standard one (≥ −0.64 V), and beyond this, the current density reaches 56.69 mA cm^{-2} mg^{-1} at −1.2 V without iR correction (Fig. 4a). After electrolysis for 1.5 h at the selected potential, the product was collected for identification using gas chromatography (GC) and nuclear magnetic resonance (NMR) (Fig. S15†). The total current densities of distorted BiOCl (Fig. 4b) are apparently higher than those of standard BiOCl nanoplates (Fig. S16a†), particularly at low potential (< −0.8 V). Remarkably, the formate selectivity at low potential (−0.5 V) is 50.42%, and then it can reach 83.99% at −0.6 V. Overall, the distorted BiOCl nanoplates maintain a high FE of nearly 90% in a wide potential

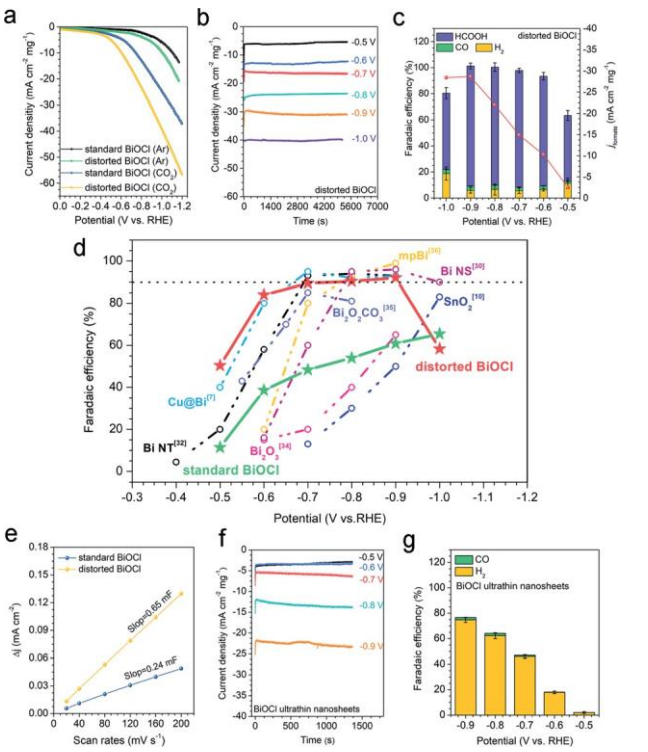

Fig. 4 CO_2RR evaluation of standard BiOCl, distorted BiOCl nanoplates and ultrathin BiOCl nanosheets. (a) Linear sweep voltammetry curves in Ar- or CO_2-saturated electrolytes. (b) Chronoamperometry results of distorted BiOCl nanoplates in CO_2-saturated electrolyte at each given potential (*versus* RHE). (c) Faradaic efficiencies of $HCOO^-$, CO, and H_2 and $HCOO^-$ partial current densities at the applied potential for 1.5 h. (d) Plot of FE for standard BiOCl, distorted BiOCl nanoplates and state-of-the-art Bi/Sn-based electrocatalysts reported in recent years. (e) ECSA measurements (R^2 ¼ 0.999). (f) Chronoamperometry results of ultrathin BiOCl nanosheets in CO_2-saturated 0.5 M $KHCO_3$ at each given potential (*versus* RHE). (g) Faradaic efficiencies of CO and H_2 at the applied potential for 1400 s.

range from −0.6 to −0.9 V, and the optimal $j_{formate}$ of −28.63 mA cm^{-2} mg^{-1} is achieved at −0.9 V (Fig. 4c). In contrast, the value of $j_{formate}$ over standard BiOCl only reaches −12.30 mA cm^{-2} mg^{-1} at −0.9 V with an FE of 57.86% (Fig. S16b†). Meanwhile, distorted BiOCl without carbon powder still maintains its high FE for HCOOH (Fig. S17†). Further, the high energy conversion efficiency (EE) of distorted BiOCl over 50% in a wide potential range from −0.6 to −0.9 V is shown in Fig. S18a†. Finally, distorted BiOCl nanoplates display a stable current density of ~32 mA cm^{-2} mg^{-1} at −0.9 V for 12 h of continuous reaction (Fig. S18b†), and the further analysis of the products indicates a steady formate faradaic efficiency of 90%. Fig. 4d and Table S3† summarize the comparison of the CO_2RR performance of standard BiOCl, distorted BiOCl nanoplates and state-of-the-art Bi/Sn-based electrocatalysts reported in recent years.[7,10,29,30,32,34–37] Overall, distorted BiOCl nanoplates with superior faradaic selectivity for formate outperform standard BiOCl and other Bi/Sn-based electrocatalysts, especially at low potential.

The electrochemically active surface area (ECSA) was calculated as shown in Fig. 4e and S19† to evaluate the intrinsic activity of standard BiOCl and distorted BiOCl nanoplates. The double-layer capacitances (C_{dl}) of standard BiOCl and distorted BiOCl are 0.24 and 0.65 mF cm^{-2}, respectively, implying that the ECSA of distorted BiOCl is 2.7 times larger than that of standard BiOCl nanoplates. The corresponding normalized current densities for formate at −0.5 V are −0.069 and −0.24 mA cm^{-2} mg^{-1}, respectively. The experimental results above demonstrate the theoretical prediction that increased intralayer $[Bi_2O_2]^{2+}$ structural distortion in thick nanoplates and the consequent increased active sites are responsible for the superior CO_2RR performance.

XRD and XPS characterization experiments are employed to explore the structural change of distorted BiOCl and standard BiOCl nanoplates after the CO_2RR (Fig. S20 and S21†). All the diffraction peaks can be indexed to a new metastable phase $Bi_2O_2CO_3$ (PDF#41-1488). The XPS spectra indicate that interlayer chlorine atoms are continuously removed until the formation of $Bi_2O_2CO_3$ during the CO_2RR. This phenomenon has been observed in BiO_x catalysts through monitoring the Bi valency by *in situ* X-ray absorption near edge structure analysis,[34,38] and the distorted BiOCl exhibits optimal activity and selectivity compared with the catalysts above. So it can be concluded that the initial intralayer $[Bi_2O_2]^{2+}$ structural distortion induced by SC CO_2 has a key role in the intrinsic activity and selectivity of layered BiOCl electrocatalysts. Moreover, compared with the initial binding energies of Bi^{3+} at 158.85 and 164.30 eV, the new peaks at 159.95 and 165. 25 eV indicate a higher oxidation state than Bi^{3+} after electrolysis. And unlike other Bi-based electrocatalysts,[34,35,37] no Bi^0 signal appears for distorted BiOCl after the CO_2RR. This further shows that positively charged Bi^{n+} is always present during electrolysis, and it can lead to favorable adsorption energy of CO_2RR intermediates.

The thickness-dependent activity for the CO_2RR. According to the foregoing theoretical analysis, thick distorted BiOCl nanoplates can provide more intralayer $[Bi_2O_2]^{2+}$ structural distortion than ultrathin nanosheets hence promoting the activity of the CO_2RR. Thus, the control experiments are performed on distorted ultrathin BiOCl nanosheets as shown in Fig. 4f and g. As expected, it is found that BiOCl ultrathin nanosheets mainly produced H_2 at the given potentials (74.75% at −0.9 V), and the overall electrochemical activity also decreased (total current density: 22 mA cm^{-2} mg^{-1} at −0.9 V). So this can confirm that the thickness-dependent structural distortion has a key role in the intrinsic activity and selectivity of layered BiOCl electrocatalysts.

Further Gibbs free energy calculations on possible reaction pathways of the CO_2RR are performed. The calculated results after solvation calibration are presented in Fig. 5, S22–S27 and Table S4†. In CO production, the formation of COOH* intermediates is the rate limiting step for the five models. Compared with perfect BiOCl (Fig. S25a†), even though the Gibbs free energies for O-deficient BiOCl (BiOCl–V_o) and Cl-deficient BiOCl are extremely decreased, the larger energy barriers still demonstrate their low activity towards CO. In the case of HCOOH production, the formation of OCHO* intermediates is the rate limiting step for perfect BiOCl (ΔG = 2.15 eV), whereas the introduction of a single Cl defect in distorted BiOCl nanoplates and ultrathin BiOCl nanosheets can change the speed-limiting step to HCOOH* by activated Bi atoms stabilizing the OCHO* intermediate, thus decreasing the energy barrier for formate formation. Strikingly, ΔG for distorted BiOCl can be further decreased when triple Cl defects are created (Fig. 5b). While the introduction of oxygen vacancies makes the energy barriers of the HCOOH pathway close to those of the H_2 pathway, *i.e.*, the H_2 and HCOOH pathways are competitive reactions for the standard BiOCl–V_o catalyst (Fig. S26†). Furthermore, ΔG for the formation of H* (intermediate to H_2) on distorted BiOCl nanoplates (0.49 eV for a single defect, 0.68 eV for triple defects) is obviously higher than that of perfect BiOCl (0.39 eV) and BiOCl–V_o (0.42 eV) (Fig. S25b†), confirming that intralayer structural distortion caused by interlayer Cl defects can efficiently suppress

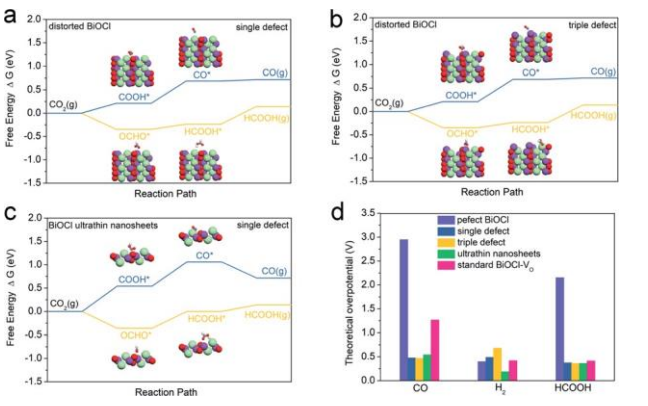

Fig. 5 Free energy diagrams (a–c) and theoretical limiting potentials for CO, HCOOH and H_2 (d) on distorted BiOCl nanoplates with a single Cl defect, distorted BiOCl nanoplates with triple Cl defects, BiOCl ultrathin nanosheets with a single Cl defect, and standard BiOCl–V_o with oxygen defects. Inset of (a–c): optimized geometric structure of various adsorbed intermediates (side view).

the dissociation of H* on the surface. Under the same degree of Cl defects, when the thickness of distorted BiOCl reduces to the atomic scale, even though the D*G* values for CO and HCOOH intermediates decrease, the HER becomes the preferential reaction (Fig. 5c and d). So it can be concluded that the activity and selectivity of the CO_2RR determined by intralayer $[Bi_2O_2]^{2+}$ structural distortion are thickness-dependent. We can rationally conclude that thick BiOCl nanoplates can afford more intralayer $[Bi_2O_2]^{2+}$ structural distortion than the ultrathin nanosheets under the same degree of Cl defects. Further, the magnitudes of the corresponding thermodynamic limiting potentials $|U_L|$ are summarized in Fig. 5d. Compared with standard BiOCl–V_o, the distorted BiOCl nanoplates with increased intralayer $[Bi_2O_2]^{2+}$ structural distortion not only suppress the product selectivity for CO and H_2, but also facilitate the formation of HCOOH. The theoretical analysis results are consistent with our experimental results.

Conclusions

In summary, supercritical CO_2-assisted fabrication of intralayer $[Bi_2O_2]^{2+}$ structural distortion in BiOCl with various thicknesses has been achieved successfully, and further the enhanced intrinsic catalytic activity correlated with increased intralayer $[Bi_2O_2]^{2+}$ structural distortion in the thick nanoplates has been demonstrated. DFT simulation indicates that intralayer $[Bi_2O_2]^{2+}$ structural distortion comes from the reduced number of interlayer Cl atoms achieved by SC CO_2 phase transition. Further thermodynamic analysis con□rms that distorted BiOCl nanoplates possess more intralayer structural distortion than ultrathin nanosheets under the identical degree of Cl defects; therefore it can efficiently suppress the generation of H_2 and CO, and guarantee the conversion of CO_2 to formate with a high selectivity (92%) and current densities in a broad-potential range from −0.6 to −0.9 V *versus* RHE. Considering the developed supercritical CO_2 technology and and the lower potential for the production of formate, this strategy of preparation of the catalyst can be expected to be extended to industrial electrosynthesis in the future.

Conflicts of interest

There are no con□icts to declare.

Acknowledgements

We are grateful to the National Natural Science Foundation of China (No. 21773216, 51173170, 21571157, 21703207), and the China Postdoctoral Science Foundation (No. 2018T110738). Theoretical calculation was carried out in the Supercomputing Center in Zhengzhou University.

References

1 M. B. Ross, P. De Luna, Y. Li, C.-T. Dinh, D. Kim, P. Yang and E. H. Sargent, *Nat. Catal.*, 2019, 2, 648–658.
2 M.-Y. Lee, K. T. Park, W. Lee, H. Lim, Y. Kwon and S. Kang, *Crit. Rev. Env. Sci. Tec.*, 2019, 1–47.
3 M. G. Kibria, J. P. Edwards, C. M. Gabardo, C. T. Dinh, A. Sei□tokaldani, D. Sinton and E. H. Sargent, *Adv. Mater.*, 2019, 31, 1807166.
4 N. Han, P. Ding, L. He, Y. Li and Y. Li, *Adv. Energy Mater.*, 2019, 1902338.
5 Y. Y. Birdja, E. Pérez-Gallent, M. C. Figueiredo, A. J. Göttle, F. Calle-Vallejo and M. T. M. Koper, *Nat. Energy*, 2019, 4, 732–745.
6 X. Zu, X. Li, W. Liu, Y. Sun, J. Xu, T. Yao, W. Yan, S. Gao, C. Wang, S. Wei and Y. Xie, *Adv. Mater.*, 2019, 31, 1808135.
7 X. Zhang, X. Sun, S.-X. Guo, A. M. Bond and J. Zhang, *Energy Environ. Sci.*, 2019, 12, 1334–1340.
8 T. Tran-Phu, R. Daiyan, Z. Fusco, Z. Ma, R. Amal and A. Tricoli, *Adv. Funct. Mater.*, 2019, 30, 1906478.
9 T. Shinagawa, G. O. Larrazábal, A. J. Martín, F. Krumeich and J. Pérez-Ramírez, *ACS Catal.*, 2018, 8, 837–844.
10 L. Fan, Z. Xia, M. Xu, Y. Lu and Z. Li, *Adv. Funct. Mater.*, 2018, 28, 1706289.
11 Z. W. Seh, J. Kibsgaard, C. F. Dickens, I. Chorkendorff, J. K. Norskov and T. F. Jaramillo, *Science*, 2017, 355, 4998.
12 R. Chattot, O. Le Bacq, V. Beermann, S. Kuhl, J. Herranz, S. Henning, L. Kuhn, T. Asset, L. Guetaz, G. Renou, J. Drnec, P. Bordet, A. Pasturel, A. Eychmuller, T. J. Schmidt, P. Strasser, L. Dubau and F. Maillard, *Nat. Mater.*, 2018, 17, 827–833.
13 L. Wang, W. Chen, D. Zhang, Y. Du, R. Amal, S. Qiao, J. Wu and Z. Yin, *Chem. Soc. Rev.*, 2019, 48, 5310–5349.
14 H. Jin, C. Guo, X. Liu, J. Liu, A. Vasileff, Y. Jiao, Y. Zheng and S. Z. Qiao, *Chem. Rev.*, 2018, 118, 6337–6408.
15 V. Kumaravel, J. Bartlett and S. C. Pillai, *ACS Energy Lett*, 2020, 5, 486–519.
16 H. Yin, Y. Dou, S. Chen, Z. Zhu, P. Liu and H. Zhao, *Adv. Mater.*, 2019, 1904870.
17 T. Sun, G. Zhang, D. Xu, X. Lian, H. Li, W. Chen and C. Su, *Mater. Today Energy*, 2019, 12, 215–238.
18 J. Li, H. Li, G. Zhan and L. Zhang, *Acc. Chem. Res.*, 2017, 50, 112–121.
19 M. J. Hÿtch, E. Snoeck and R. Kilaas, *Ultramicroscopy*, 1998, 74, 131–146.
20 J. H. Warner, E. R. Margine, M. Mukai, A. W. Robertson, F. Giustino and A. I. Kirkland, *Science*, 2012, 337, 209–212.
21 C. Lv, G. Chen, X. Zhou, C. Zhang, Z. Wang, B. Zhao and D. Li, *ACS Appl. Mater. Interfaces*, 2017, 9, 23748–23755.
22 A. Puthirath Balan, S. Radhakrishnan, R. Kumar, R. Neupane, S. K. Sinha, L. Deng, C. A. de los Reyes, A. Apte, B. M. Rao, M. Paulose, R. Vajtai, C. W. Chu, G. Costin, A. A. Martí, O. K. Varghese, A. K. Singh, C. S. Tiwary, M. R. Anantharaman and P. M. Ajayan, *Chem. Mater.*, 2018, 30, 5923–5931.
23 J. Ye, C. Liu, D. Mei and Q. Ge, *ACS Catal.*, 2013, 3, 1296–1306.
24 Z. Xia and S. Guo, *Chem. Soc. Rev.*, 2019, 48, 3265–3278.
25 D. Kim, C. Xie, N. Becknell, Y. Yu, M. Karamad, K. Chan, E. J. Crumlin, J. K. Norskov and P. Yang, *J. Am. Chem. Soc.*, 2017, 139, 8329–8336.

26 J. I. Langford and D. Louër, *Rep. Prog. Phys.*, 1996, 59, 131–234.
27 P. Deng, H. Wang, R. Qi, J. Zhu, S. Chen, F. Yang, L. Zhou, K. Qi, H. Liu and B. Y. Xia, *ACS Catal.*, 2019, 10, 743–750.
28 A. Azizi, X. Zou, P. Ercius, Z. Zhang, A. L. Elias, N. Perea-Lopez, G. Stone, M. Terrones, B. I. Yakobson and N. Alem, *Nat. Commun.*, 2014, 5, 4867.
29 H. Zhang, Y. Ma, F. Quan, J. Huang, F. Jia and L. Zhang, *Electrochem. Commun.*, 2014, 46, 63–66.
30 N. Han, Y. Wang, H. Yang, J. Deng, J. Wu, Y. Li and Y. Li, *Nat. Commun.*, 2018, 9, 1320.
31 M. Pourbaix, *Biomaterials*, 1984, 5, 122–134.
32 Q. Gong, P. Ding, M. Xu, X. Zhu, M. Wang, J. Deng, Q. Ma, N. Han, Y. Zhu, J. Lu, Z. Feng, Y. Li, W. Zhou and Y. Li, *Nat. Commun.*, 2019, 10, 2807.
33 X. Zheng, P. De Luna, F. P. García de Arquer, B. Zhang, N. Becknell, M. B. Ross, Y. Li, M. N. Banis, Y. Li, M. Liu, O. Voznyy, C. T. Dinh, T. Zhuang, P. Stadler, Y. Cui, X. Du, P. Yang and E. H. Sargent, *Joule*, 2017, 1, 79427805.
34 S. Liu, X. F. Lu, J. Xiao, X. Wang and X. W. D. Lou, *Angew. Chem., Int. Ed.*, 2019, 58, 13828–13833.
35 Y. Zhang, X. Zhang, Y. Ling, F. Li, A. M. Bond and J. Zhang, *Angew. Chem., Int. Ed.*, 2018, 57, 13283–13287.
36 H. Yang, N. Han, J. Deng, J. Wu, Y. Wang, Y. Hu, P. Ding, Y. Li, Y. Li and J. Lu, *Adv. Energy Mater.*, 2018, 8, 1801536.
37 F. P. Garcia de Arquer, O. S. Bushuyev, P. De Luna, C. T. Dinh, A. Sei□tokaldani, M. I. Saidaminov, C. S. Tan, L. N. Quan, A. Proppe, M. G. Kibria, S. O. Kelley, D. Sinton and E. H. Sargent, *Adv. Mater.*, 2018, 30, 1802858.
38 C. W. Lee, J. S. Hong, K. D. Yang, K. Jin, J. H. Lee, H.-Y. Ahn, H. Seo, N.-E. Sung and K. T. Nam, *ACS Catal.*, 2018, 8, 931–937.